



## **System Design and Modelling of an Air-breathing Electric Propulsion Spacecraft**

Gunaltay, Hamza Eren; Moloney, Rachel; Tisaev, Mansur; Baresi, Nicola; Underwood, Craig Ian; Lucca Fabris, Andrea; Marxen, Olaf; et.al.

<https://openresearch.surrey.ac.uk/esploro/outputs/conferenceProceeding/System-Design-and-Modelling-of-an/991034266402346/filesAndLinks?index=0>

---

Gunaltay, H. E., Moloney, R., Tisaev, M., Baresi, N., Underwood, C. I., Lucca Fabris, A., Marxen, O., & Gini, F. (2025). System Design and Modelling of an Air-breathing Electric Propulsion Spacecraft. <https://doi.org/>  
Document Version: Author's Accepted Manuscript

---

# System Design and Modelling of an Air-breathing Electric Propulsion Spacecraft

IEPC-2025-348

*Presented at the 39th International Electric Propulsion Conference, Imperial College London, London,  
United Kingdom  
14-19 September 2025*

Hamza Eren Gunaltay\*, Rachel Moloney, Mansur Tisaev<sup>†</sup>, Nicola Baresi,  
Craig Underwood, Andrea Lucca Fabris  
*Surrey Space Centre, University of Surrey, Guildford, GU2 7XH, UK*

Olaf Marxen  
*Centre for Aerodynamics, Aerospace and Automotive Engineering,  
University of Surrey, Guildford, GU2 7XH, UK*

*and*

Francesco Gini  
*European Space Operation Centre, European Space Agency, Darmstadt, 64293, Germany*

Air-breathing electric propulsion (ABEP) systems offer a potential solution for sustained spacecraft operations in Very Low Earth Orbit (VLEO), by utilizing atmospheric particles as propellant, thereby reducing dependence on onboard fuel. This work presents the design, feasibility, and orbital performance of the ABEP spacecraft EULO, intended to operate near 200 km with a high resolution optical Earth observation payload. A preliminary 550 kg spacecraft was designed to meet mass, power, and aerodynamic constraints while fitting within a UK based launcher, RS-1. The orbital performance of the satellite was simulated with a high-fidelity propagator coupled with a panel based aerodynamic force estimation method using gas-surface interaction models evaluated at each time step. This geometric framework, compared to a classic cannonball model, enables modelling of the spacecraft's attitude, which in this study was held constant and either aligned with the orbital velocity or the local flow. Simulations on a generic ABEP spacecraft highlighted that misalignments with the relative flow can significantly affect orbital stability, with some configurations experiencing de-orbiting due to such misalignments. Furthermore, the EULO spacecraft demonstrated sustained a simulated flight at 255 km, achieving a theoretical ground sampling distance of 0.38 m and requiring the intake to have a collection efficiency of 50%. Nevertheless, uncertainties in the aerodynamic modelling suggests that improving thruster performance will be essential to mitigate these uncertainties.

---

\*Postgraduate researcher, Surrey Space Centre, h.gunaltay@surrey.ac.uk  
†Current affiliation: Oregon State University, Corvallis, OR97331, USA



## Nomenclature

$A$	Area
$AR_i$	Intake aspect ratio
$C_{nm}, S_{nm}$	Spherical harmonic coefficients
$c_p$	Pressure coefficient
$c_\tau$	Shear coefficient
$\delta$	Incidence flow angle
$e$	Orbital eccentricity
$GM$	Gravitational parameter
$k_\eta$	Rate of change of collection efficiency
$m$	Mass of the body / Order of spherical harmonics
$n$	Mean motion / Degree of spherical harmonics
$P_{nm}(\cos \theta)$	Legendre polynomial
$r$	Radial distance
$\rho_\infty$	Free-stream density
$R_\oplus$	Radius of Earth
$s$	Molecular speed ratio
$\sigma_N$	Normal accommodation coefficient
$\sigma_T$	Tangential accommodation coefficient
$T_\infty$	Free-stream temperature
$T_w$	Wall temperature
$u_b$	Acceleration along orbit normal
$u_v$	Acceleration along velocity axis
$v_\infty$	Free-stream velocity
$V$	Gravitational potential
$\vec{a}_{aero}$	Aerodynamic acceleration
$\vec{n}$	Normal direction
$\vec{\tau}$	Shear direction
$\beta$	Compression ratio
$\dot{r}_p$	Rate of change of periapsis
$\eta_c$	Intake collection efficiency
$\nu$	True anomaly
$\phi$	Longitude
$\theta$	Colatitude



## Acronyms

AABB	Axis-Aligned Bounding Box
ABEP	Air-Breathing Electric Propulsion
ADCS	Attitude Determination and Control Subsystem
AoA	Angle of Attack
BVH	Bounding Volume Hierarchy
CAD	Computer-aided design
DSMC	Direct Simulation Monte Carlo
EULO	Enabling Ultra Low Orbits
GSD	Ground Sample Distance
GSI	Gas Surface Interaction
RTP	Ray Tracing Panel
SRP	Solar Radiation Pressure
SSC	Surrey Space Centre
SSTL	Surrey Satellite Technologies Ltd.
TPMC	Test Particle Monte Carlo
UKSA	United Kingdom Space Agency
VLEO	Very Low Earth Orbit
VNB	Velocity–Normal–Binormal
WRF	Wind Reference Frame



## I. Introduction

Traditional electric propulsion systems are constrained by their limited onboard propellant supply, which in turn restricts their operational lifespan. Air-Breathing Electric Propulsion (ABEP) is an emerging technology designed for spacecraft operating at Very Low Earth Orbit (VLEO), typically defined as altitudes between 100 and 450 km.<sup>1</sup> These spacecraft offer a sustainable alternative by utilising upper atmospheric particles as a theoretically infinite source of propellant. In an ABEP system, free atmospheric particles are collected using an intake mechanism. These intake mechanisms are generally classified according to their particle capture mechanism: designs that solely rely on static geometric features are considered passive, whereas those incorporating moving components such as turbo-molecular pumps are classified as active. In addition to capturing particles, the intake system is also responsible for slowing the particles down from relative orbital velocities and compressing them for use as propellant. After passing the intake unit, captured and compressed particles are fed into an electric propulsion unit, where they are accelerated again to generate a net thrust.

However, in VLEO where an ABEP thruster can operate, the satellite experiences significant aerodynamic drag, which must be actively counteracted by the propulsion system. In addition to drag, the proximity to Earth increases the satellite's susceptibility to non-spherical gravity field of the Earth. These combined effects necessitate the use of a high-fidelity orbital propagator. Many existing software tools, such as GMAT,<sup>2</sup> rely on cannonball atmospheric drag models, which fail to capture both the influence of spacecraft attitude and the complex nature of orbital aerodynamics. Therefore, it necessitates the development of new tools that could capture these effects. Despite these challenges, VLEO offers unique benefits, including improved resolution for optical payloads, reduced communication latency, and the advantage of natural de-orbiting.<sup>1,3</sup>

This paper is organised as follows: Section II describes the Enabling Ultra Low Orbits (EULO) spacecraft designed to operate in VLEO and the associated design considerations while Section III discusses the high-fidelity orbit propagator and the aerodynamic estimation methods used in this research, along with key considerations, and a discussion of the associated limitations. Section IV presents preliminary findings on the VLEO and ABEP satellites, simulated using a GOCE<sup>4</sup> like satellite and specifications of an ABEP thruster working with N<sub>2</sub>-O<sub>2</sub> mixtures.<sup>5</sup> Building upon the findings of this section, Section V demonstrates the detailed aerodynamics and the flight envelope of the EULO spacecraft. Finally, Section VI provides conclusions from this study.

## II. Air-Breathing Satellite System Design

The spacecraft design is primarily dictated by the mission objectives and payload requirements. In this study, the payload chosen was an optical Earth observation instrument designed to be operating in a 200 km circular orbit. Furthermore, the satellite design was carried out with adaptability in mind, in order to ensure suitability for potential future constellation deployments. Additionally, at such low altitudes, compactness is critical, as protruding structures significantly increase aerodynamic drag. To mitigate this, the telescope was housed within the spacecraft body, with a 45° mirror used to direct incoming light to the optical system. A Cassegrain configuration was selected despite its complexity, as it minimises the required volume while meeting the performance requirements. A schematic of this configuration was illustrated in Fig. 1. The primary objective of the payload was to achieve a Ground Sample Distance (GSD) of approximately 0.3 m at the red end of the panchromatic band. According to the Rayleigh criterion, this necessitated a minimum aperture diameter of about 53 cm. Allowing margin for fittings and shrouds, the aperture was rounded to 60 cm.

In addition to the optical payload and reflecting mirror, the spacecraft must also accommodate the bus subsystems, auxiliary sensors, and the intake system required for the ABEP thruster. Preliminary estimates, consistent with previous studies,<sup>1,7</sup> indicated that at least two thrusters providing 7 mN of thrust each would be necessary to maintain orbit. Initially, for additional robustness, a third thruster of equivalent performance was included as a design margin. This configuration required a relatively wide and elongated intake. Initial designs assumed an intake diameter of approximately 1 m with a length of about 1.5 m. Recent findings have shown that maintaining orbits at such low altitudes would necessitate an active compression system,<sup>7</sup> which would further increase the system size. To prevent excessive growth, a constraint was imposed that the spacecraft must remain compatible with UK-based launchers. Specifically, the RS1 launch vehicle was selected as the baseline reference for defining the spacecraft's maximum allowable dimensions.<sup>8</sup>



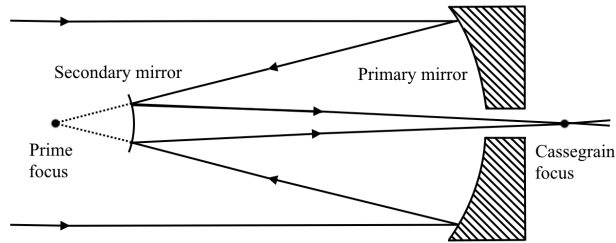


**Figure 1. Cassegrain Telescope Schematic<sup>6</sup>**

Following the iterative design process and the choice of the launch vehicle, initial spacecraft had to be modified to avoid the excessive volume that would have been occupied by a single large intake. Instead, three separate intakes were adopted, each connected to an individual thruster. To ensure adequate airflow to the thrusters, the diameter of each intake was scaled to approximately 72 cm. This configuration necessitated an increase in the spacecraft's overall diameter. Similarly, to efficiently utilise the payload fairing of the RS1 launch vehicle, a circular cross-section of 1.6 m in diameter was selected. However, this configuration resulted on a larger satellite than initial intentions which made the third thruster a necessity rather than redundancy. Furthermore, the use of three intakes motivated the adoption of a nonagonal perimeter for the spacecraft structure, which provided geometric symmetry and optimised use of the available volume. The nonagonal cross-section was defined such that its innermost circumscribed circle had a diameter of 1.6 m.

The RS1 payload fairing, given the diameter of 1.6 m, permits a maximum spacecraft height of roughly 3 m. Within this volume, the intake system occupies about 1 m length. Modular avionics boxes, mounted on the back plate, are estimated to require an additional 20 cm. This allocation leaves approximately 1.8 m available for the payload and optical assembly. Taking the diameter of the 45° mirror to be 65 cm for the optical assembly, this leaves about 1.15 m for the telescope itself. With a Cassegrain configuration, this length is sufficient to accommodate an optical system with an effective focal length of about 6.7 m. Coupled with a detector pixel size of  $10 \mu\text{m}$ , the system yields a ground sample distance of roughly 0.3 m, with an f-number of approximately f/11.

The authors would like to acknowledge that dedicated research on intake design has been carried out; however, as this work has not yet concluded, it is not presented in this paper. For representation purposes in the present study, parabolic bucket-type intakes were adopted in the illustrative configurations in following Fig. 2 and 3.

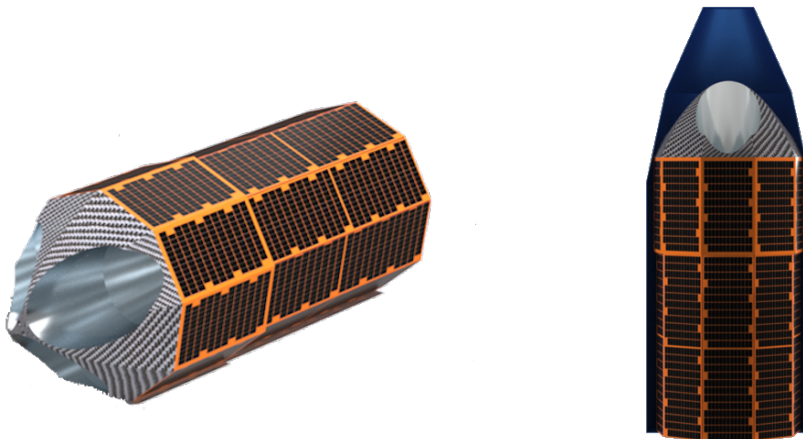


**Figure 2. Stowed configuration of the ABEP spacecraft. The figure shows the satellite accommodated within the RS1 fairing (right) and outside the fairing (left).**

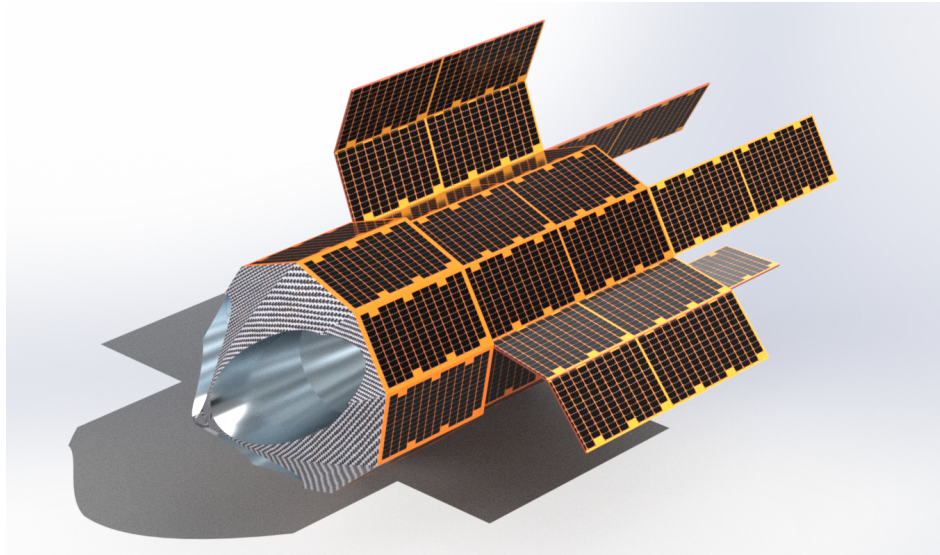


**Figure 3.** ABEP spacecraft “EULO” in deployed configuration.

### A. Power Systems

Preliminary estimates indicate that the three thrusters require approximately 2 kW of DC electrical power during operation. To ensure uninterrupted operation, the spacecraft must also be able to withstand a worse case eclipse periods of up to 37 minutes. This necessitates on board batteries. The battery system is sized such that three units, mounted symmetrically on the nonagonal body, provide a nominal continuous supply of 1 kW. To accommodate peak demand, the system is designed to deliver up to 3 kW if required.

For the solar panels, a panel size of  $100 \times 55$  cm was assumed with 150 quad junction solar cells. Under direct illumination, with a nominal solar flux of  $1367 \text{ W/m}^2$  and cell efficiency of 32%, each panel provides approximately 195 W of power. This implies that a single side panel of the nonagonal satellite could provide up to 585 W of power. While the entire spacecraft body would theoretically yield 5265 W, when the Sun illumination is normal to one side, shadowing and limited rays reaching the panels reduce the output to roughly 1.7 kW. Therefore it necessitates the use of additional deployable solar panels.

To address this, the design includes three cranked deployable panels, each accommodating four arrays, with two of the arrays bent at an interior angle of  $140^\circ$ . When illuminated normally, these panels would be capable of generating approximately 733 W. In addition, a motorised solar tail unit provides a further 390 W. Altogether, the configuration allows for a worst-case power generation of about 2.8 kW. Moreover, the motorised solar tail units can also contribute to active attitude control. Nevertheless, the authors would like to acknowledge that the motorised panels behind the propulsion unit may introduce disturbances due to plasma plume interactions. The issue remains under investigation and will be assessed in future work. This was further illustrated in Fig. 3.

### B. Final Spacecraft Configuration

Due to the inclusion of three intakes in the spacecraft design, majority of the frontal surface is covered by structural walls rather than intake openings. Therefore, a nose cone was introduced at the front of the spacecraft. The RS1 fairing allows for a sharp nose cone with a height of up to 50 cm. Preliminary investigations using the panel-based drag model, with both conical and parabolic geometries, indicated that a parabolic profile offers slightly improved aerodynamic performance. Consequently, the final configuration adopted a parabolic nose cone. To accommodate the intake openings, the relevant sections of the nose were cut flat. Finally, based on preliminary subsystem estimates, including structure, power systems, intake assemblies, Attitude Determination and Control Subsystem (ADCS), avionics stacks, the total platform dry mass is expected to be approximately 550 kg. The final ABEP spacecraft EULO is illustrated in Fig. 2 and 3. Figure 2 shows the spacecraft with the panels stowed (left) and accommodated within the fairing volume (right), while Figure 3 depicts the spacecraft in its deployed configuration.

### III. Orbit Propagation in Very Low Earth Orbit

An orbital propagator is a tool in astrodynamics for predicting the future position and velocity of an orbiting object by numerically propagating its equations of motion.<sup>7</sup> In VLEO, orbital perturbations are dominated by aerodynamic drag resulting from interactions between the spacecraft and the upper atmospheric particles, as well as gravitational disturbances arising from the Earth's non-spherical shape and the third body influence of the Moon and the Sun.<sup>9</sup> To capture these effects, this study employs a high-fidelity propagator previously developed by the authors.<sup>7</sup> The following subsections describe the dynamics model implemented in the tool, along with the improvements introduced for this study.

#### A. Perturbations Due to Planetary Bodies

The gravitational influence of third bodies, specifically the Moon and the Sun, introduces perturbations that affect both the satellite's orbit and the motion of the Earth itself. The gravitational potential,  $V_{tb}$ , created by these third bodies is determined from the relative position of the external body with respect to the satellite's position. Equation (1) highlights the perturbing potential of the third-body where  $GM_{tb}$  is the gravitational parameter of the third body,  $r$  is the distance from satellite to the main planetary body,  $r_{tb}$  is the distance from main planetary body to the third-body. The bold symbols denote their corresponding vector representations.

$$V_{tb} = \frac{GM_{tb}}{r_{tb}} \left( \frac{r^2}{r_{tb}^2} - 3 \frac{(\mathbf{r} \cdot \mathbf{r}_{tb})}{r_{tb}^2} \right) \quad (1)$$

In addition to third body effects, motion in VLEO is subject to strong perturbations due to the non-spherical gravity field of Earth. Equation (2) expresses the gravitational potential of the main planetary body, Earth, where,  $GM$  is the gravitational parameter of the Earth,  $R_{\oplus}$  is Earth's mean equatorial radius,  $r, \theta, \phi$  are spherical coordinates (radial distance, colatitude, longitude),  $C_{nm}, S_{nm}$  are spherical harmonic coefficients of degree  $n$  and order  $m$  and  $P_{nm}(\cos \theta)$  are the associated Legendre polynomials.<sup>10</sup>

$$V_{sh}(r, \theta, \phi) = \frac{GM}{r} \left[ 1 - \sum_{n=2}^{\infty} \sum_{m=0}^n \left( \frac{R_{\oplus}}{r} \right)^n \left( C_{nm} \cos(m\phi) + S_{nm} \sin(m\phi) \right) P_{nm}(\cos \theta) \right] \quad (2)$$

The coefficients for degrees and orders of the spherical harmonics were obtained from GGM05C.<sup>11</sup> All frame transformations and the computation of distances from the central body to other planetary bodies were performed using SPICE kernels.<sup>12</sup>

#### B. Atmospheric Drag in the Rarefied Regime

The accelerations induced by atmospheric forces are expressed in Eq. (3) where  $\rho_{\infty}$  is the free-stream density,  $v_{\infty}$  is the free stream velocity,  $A_{ref}$  is a reference area,  $\vec{C}_F$  is the non-dimensional force coefficient,  $m$  is the mass of the spacecraft and  $\vec{F}$  is the aerodynamic force vector. Many software tools available in the literature estimate the drag forces using a "cannonball" drag model with a constant drag force coefficient. However, to obtain a representative drag coefficient for VLEO conditions, it is necessary to vectorise the coefficient, thereby allowing the influence of spacecraft attitude to be incorporated.

$$\vec{a}_{aero} = \frac{\vec{F}}{m} = \frac{1}{2} \frac{\rho_{\infty} v_{\infty}^2 A_{ref} \vec{C}_F}{m} \quad (3)$$

Moreover, the flow conditions in VLEO differ from those encountered by conventional aircraft, a more detailed explanation can be found in Ref. 1. Furthermore, estimating the aerodynamic acceleration requires accurate knowledge of the atmospheric density. Consistent with previous studies,<sup>1,7</sup> the present work also employs the NRLMSISE-00 atmospheric density model<sup>13</sup> which estimates atmospheric density as a function of location, day of the year, and space weather conditions such as solar and geomagnetic activity. Moreover, this paper also employed a panel-based force estimation model,<sup>7</sup> in which the spacecraft is subdivided into  $n$  flat panels to compute the aerodynamic forces acting on its surface. The total aerodynamic force is then defined by Eq. (4) where,  $n'$  is the number of panels directly exposed to the flow,  $c_{\tau}$  is the shear force coefficient,  $c_p$  is the pressure force coefficient,  $\vec{\tau}$  is the unit vector in the shear force direction,  $\vec{n}$  is the unit vector in the normal force direction and  $i$  indexes the  $i^{\text{th}}$  panel.



$$\vec{F} = \frac{\rho_\infty v_\infty^2}{2} \sum_{i=1}^{n'} (c_{\tau,i} \vec{\tau}_i - c_{p,i} \vec{n}_i) A_i \quad (4)$$

For each exposed (non-shadowed) panel, the aerodynamic force coefficients are computed using Gas Surface Interaction (GSI) models, which describe how individual gas particles interact with a surface at the molecular level. Detailed descriptions of these models can be found in Ref. 14. Following the approach used in previous research,<sup>1</sup> the present work employs Schaaf's<sup>15</sup> GSI model, expressed in Eq. (5) and Eq. (6). In these expressions,  $\sigma_N$  and  $\sigma_T$  are the normal and tangential momentum accommodation coefficients, respectively,  $s$  is the molecular speed ratio,<sup>1</sup>  $\delta$  is the angle between the surface normal and the free-stream velocity vector,  $T_w$  is the wall temperature,  $T_\infty$  is the free-stream temperature, and  $\text{erf}(\cdot)$  denotes the error function. To maintain consistency with the previous research,<sup>1</sup> tangential and normal momentum accommodation coefficients were assumed to be equal to each other.

$$c_p = \frac{1}{s^2} \left( \left( \frac{2 - \sigma_N}{\sqrt{\pi}} s \cos(\delta) + \frac{\sigma_N}{2} \sqrt{\frac{T_w}{T_\infty}} \right) e^{-s^2 \cos^2(\delta)} + \left( [2 - \sigma_N] \left[ s^2 \cos^2(\delta) + \frac{1}{2} \right] + \frac{\sigma_N}{2} \sqrt{\frac{\pi T_w}{T_\infty}} s \cos(\delta) \right) \times (1 + \text{erf}(s \cos(\delta))) \right) \quad (5)$$

$$c_\tau = \frac{\sigma_T \sin(\delta)}{s \sqrt{\pi}} (\exp(-s^2 \cos^2(\delta)) + s \sqrt{\pi} \cos(\delta) (1 + \text{erf}(s \cos(\delta)))) \quad (6)$$

Similarly, the free-stream (relative) velocity of particles impacting the spacecraft was computed by incorporating atmospheric wind contributions from the HWM07 model.<sup>7</sup> Two spacecraft attitudes were considered in this study. First, the spacecraft attitude was defined with a constant alignment to the Velocity–Normal–Binormal (VNB) frame<sup>7</sup> where the x-axis points towards the orbital velocity vector, the y-axis points toward the direction of the orbital angular momentum vector and the z-axis completes the right-triad. Second, the attitude was expressed in the Wind Reference Frame (WRF), defined by a rotation from the VNB frame based on the satellite's angle of attack and sideslip angle, thereby generating zero angle of attack and zero sideslip. A comparison of these frame alignments were presented in the following sections and illustrated in Fig. 4 and 5.

### C. Shadowing Algorithm

The shadow detection algorithm employed in this work is based on the implementation available in ADBSat,<sup>14</sup> which determines whether a given panel is exposed to the free-stream flow, or occluded by other spacecraft

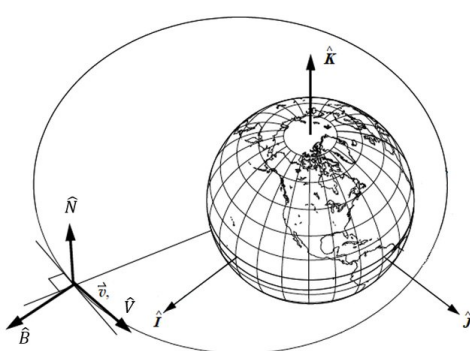


Figure 4. Illustration of the VNB frame.<sup>16</sup>

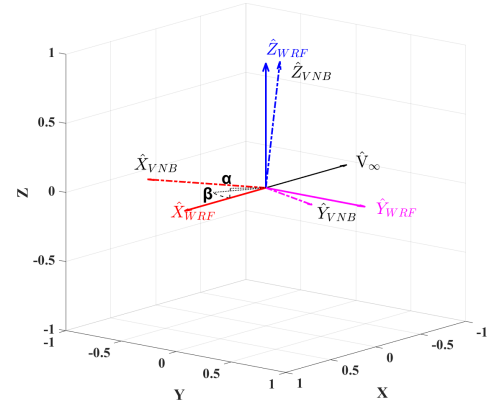


Figure 5. Illustration of the WRF frame.

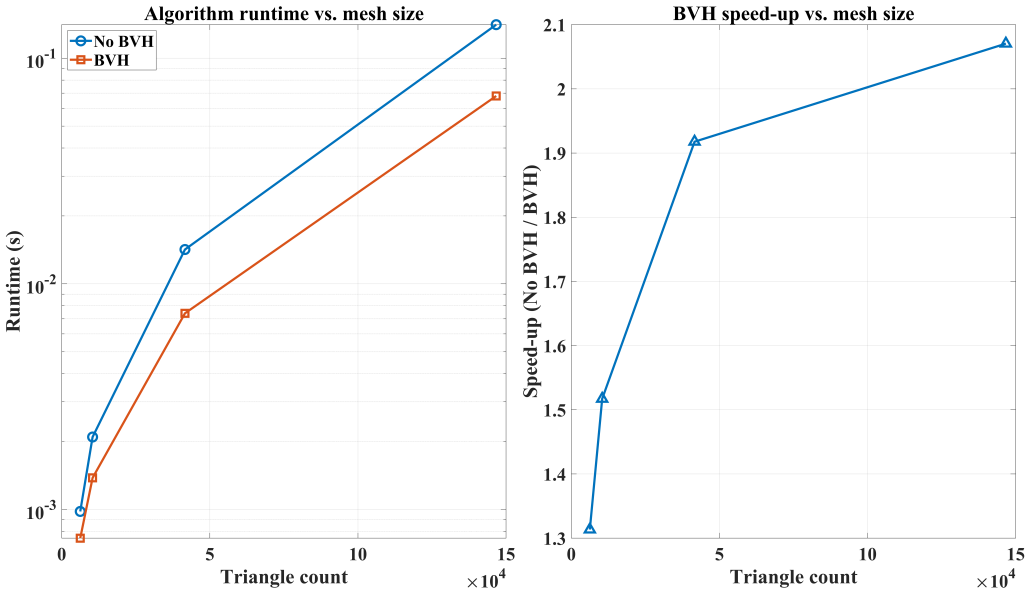


Figure 6. Comparison of runtimes with and without BVH acceleration.

surfaces, using a fast pseudo ray-tracing approach. Although the original implementation is efficient for single evaluation, it becomes a computational bottleneck in orbital propagation, where the algorithm must be executed repeatedly at each integration step, particularly when the spacecraft attitude evolves with time. For simple and small geometries, the effect of shadowing computations is negligible since the number of surface panels is relatively small. However, for more complex spacecraft meshes, the computational cost becomes significant. This limitation could be addressed either by employing a lookup table, where data are precomputed and attitude angles are coarsely rounded to the nearest available estimate, or alternatively through the use of a Bounding Volume Hierarchy (BVH), which has been shown to substantially accelerate ray-tracing algorithms.<sup>17</sup>

BVH is a technique commonly used in computer graphics, where geometric objects are organised into a hierarchical tree of simple nested bounding volumes such as spheres or cubes. During ray-tracing, this structure enables entire groups of objects to be excluded from consideration if their bounding volume is not intersected, thereby reducing the number of costly intersection tests. This approach is particularly effective for high-resolution meshes, where the computational expense of direct intersection checks can otherwise dominate the runtime.<sup>17</sup> A simple bounding box methodology, known as the Axis-Aligned Bounding Box (AABB), is widely used in general ray-tracing applications. It works by enclosing objects within a small rectangular box, allowing algorithm to quickly discard rays that do not intersect those boxes. Similar approaches have also been applied in the literature, where AABB methods were previously implemented for Solar Radiation Pressure (SRP) computations and demonstrated to be effective.<sup>18</sup>

In this study, the AABB filter was also implemented, as it could be directly integrated into the original ADBSat pseudo ray-tracing algorithm. Since the original approach from Ref. 14 already reduces the shadowing problem to two dimensions, an AABB was constructed for each potentially shadowing back-facing triangle by enclosing it within the smallest axis-aligned rectangle in the  $y$ - $z$  plane of the WRF frame, as its  $x$ -axis is aligned with the relative flow vector. During the pseudo ray-tracing procedure, if the centroid of front facing panel does not fall within this bounding box, the intersection check is skipped and the algorithm proceeds to the next panel. The algorithm was also ported to a CUDA<sup>19</sup> environment, with the AABB construction performed on the CPU, as pre-computing them on the host was more efficient than generating them directly on the GPU. The remaining shadowing procedure was executed on the GPU to take advantage of parallelisation.

The results in Fig.6 demonstrate the runtime differences between the preliminary algorithms executed with and without BVH acceleration. The comparison was performed using the satellite geometry described in Sec. II, evaluated at zero degrees angle of attack and side-slip. It should be noted that the speed-up achieved with BVH depends on both the geometric complexity and the mesh resolution, with greater improvements



observed for larger and more detailed meshes. All computations were performed on an NVIDIA RTX A4500 GPU through a MATLAB MEX interface implemented in C++/CUDA. Both implementations were verified against the original ADBSat algorithm for the satellite geometry defined in Sec. II. Across randomly generated attitude cases, both versions produced consistent results, with only minor discrepancies observed for configurations where the angle of attack or sideslip was smaller than  $0.1^\circ$ . These discrepancies, however, always corresponded to less than 0.01% of the spacecraft's total surface area. These differences are attributed to numerical tolerances associated with nearly parallel surfaces, as noted in the original ADBSat study.<sup>14</sup> The runtimes presented on the Fig. 6 correspond to averages over 1000 integration steps. Further discussions on the general results of the algorithm, and its associated limitations are provided in Sec. IV.

#### D. Air-Breathing Propulsion Considerations

In addition to the models described in the previous sections, implementation of an ABEP system introduces further constraints and perturbations. One of the most significant constraints is the presence of an intake. Since the intake is designed to capture atmospheric particles, the resulting particle-surface interactions slightly differ due to multi scattering. Furthermore, an ABEP system must also decelerate the incoming particles, which further modifies the perturbations generated by the spacecraft. Following the approach in a previous study,<sup>1</sup> these effects are represented through the concept of collection efficiency,  $\eta_c$ , defined as the fraction of particles reaching the downstream end of the collection unit relative to those entering the intake.

The fraction of particles that do not reach the end of the intake unit is assumed to contribute to drag in the same manner as interactions with the external spacecraft surfaces. This effective reduction in exposed surface area is represented in the Computer-aided design (CAD) model by scaling down the corresponding panel areas. The remaining particles that reach the downstream end of the intake are assumed to fully exchange their momenta to the spacecraft, and the resulting perturbation is given by Eqn. (7). In this expression,  $A_{\text{intake}}$  denotes the effective cross-sectional area of the intake, while  $\hat{i}_1$  represents the unit vector aligned with the spacecraft body x-axis.

$$\vec{a}_{\text{intake}} = \frac{\eta_c \rho_\infty A_{\text{intake}} v_\infty}{m} \hat{i}_1 \quad (7)$$

Furthermore, to estimate the passive compression ratio, the formulation presented in Ref. 20 was adopted, consistent with the approach used in previous studies,<sup>1,7</sup> and is expressed in Eq. (8). In this equation,  $\beta$  denotes the passive compression ratio, while  $AR_i$  is the intake aspect ratio. Unlike previous studies, the present work further introduces a variability in the collection efficiency to account for misalignment between the intake axis and the free-stream velocity vector. This effect is represented by a simple linear model, expressed by Eq. (9) where  $\eta_{c,0}$  is the nominal collection efficiency at zero misalignment,  $\delta$  is the misalignment angle, and  $k_\eta$  is a proportionality coefficient defining the rate of efficiency reduction with increasing misalignment. Nevertheless, the variation in collection efficiency is dependent on factors such as the intake geometry and flow conditions. To simplify the present analysis, the proportionality coefficient was assumed to correspond to a reduction of 0.01 per degree of misalignment. The detailed investigation of these effects was left as future work.

$$\beta = 0.87 \beta_0 (0.244 + 0.33 \ln(AR_i)) \left( \frac{189}{T_w + 33} + 0.435 \right) (1 - 1.625 \eta_c) \quad (8)$$

$$\eta_c(\delta) = \eta_{c,0} - \delta k_\eta \quad (9)$$

## IV. Flight Simulation and Orbit-Keeping with an Air-Breathing Thruster

### A. Orbit control

Orbital control in the VLEO environment poses unique challenges due to the continuous effect of atmospheric drag. Thrusting at inappropriate intervals, such as near periapsis, primarily influences the apoapsis and can have an overall detrimental effect on the orbit stability. In previous research,<sup>7</sup> a control parameter was introduced based on Gauss's variational equations,<sup>21</sup> specifically derived from the rate of change of the periapsis, as defined in Eqn. (10). In this expression,  $n$  represents the mean motion of the satellite,  $\nu$  is the true anomaly, and  $e$  is the orbital eccentricity. The terms  $u_v$  and  $u_b$  denote the thrust accelerations



along the velocity and orbit-normal directions, respectively. Assuming a spacecraft attitude alignment to the VNB frame, the thrust vector would be aligned only with the orbital velocity direction. Consequently, the orbit-plane component  $u_b$  was set to zero. The remaining term, excluding the mean motion contribution, was then defined as the control parameter  $k_p$ , as given in Eqn. (11).

$$\dot{r}_p = \frac{2}{n} \sqrt{\frac{(1-e)^3(1-\cos\nu)^2}{(1+2e\cos\nu+e^2)(1+e)}} u_v - \frac{r}{\nu} \sin\nu u_b \quad (10)$$

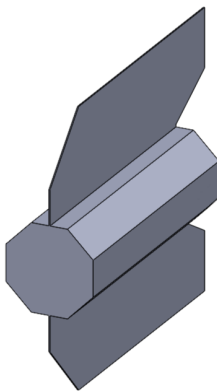
$$k_p = 2 \sqrt{\frac{(1-e)^3(1-\cos\nu)^2}{(1+2e\cos\nu+e^2)(1+e)}} \quad (11)$$

For orbit control, the previous study<sup>7</sup> identified a threshold value of 0.3 for the control parameter, with the thruster getting activated whenever this value is exceeded. In the present work, the same parameter is adopted for control. Similarly, the thruster operating conditions defined in Ref. 1 were also applied, setting the lower limits of the mass flow rate and number density to 6 sccm and  $10^{18} \text{ m}^{-3}$ , respectively. The authors acknowledge that in Ref. 7, a constant mass flow rate of 0.1 mg/s was used, independent of the atmospheric composition. During the subsequent trials, it was observed that the 6 sccm limit produced more optimistic results compared to using an approximate mg/s mass flow rate, specifically in edge cases where sustained flight was marginal. A more detailed discussion of this effect as well as the influence of control parameter on the WRF frame, is provided in the following section.

## B. Flight Simulations

A GOCE-like spacecraft configuration was first employed to demonstrate the differences arising from the attitude alignment in the WRF frame and to study the influence of the varying collection efficiency. The spacecraft model used in the propagation is illustrated in Fig. 7. A total solar panel area of  $1.4 \text{ m}^2$  was assumed, along with 200 kg spacecraft mass.<sup>7</sup> Similarly, the intake was represented as a reduction in the frontal area for varying intake diameters as discussed in Sec. III. Moreover, for this analysis, due to the simplicity of the shape, no shadowing algorithm was utilised.

The simulations were carried out using the GGM05C gravity field truncated at degree and order  $50 \times 50$ .<sup>11</sup> Third-body perturbations from the Sun and Moon were modelled as point masses. Aerodynamic effects were estimated with an accommodation coefficient of 0.9 and a wall temperature of 400 K. Solar and geomagnetic activity were held constant, with a solar flux of 140 sfu ( $1.4 \times 10^{-20} \text{ W m}^{-2} \text{ Hz}^{-1}$ ) and a geomagnetic index of  $A_p = 15$ . All simulations were initialized at the J2000 epoch, with the corresponding state vector provided in Table 2. Furthermore, the thruster was assumed to be a RIT-10 tested with N<sub>2</sub>-O<sub>2</sub> mixtures<sup>5</sup> producing a constant thrust of 7.16 mN when operational.



Component	X	Y	Z
Position [km]	146.7	-700.7	6529.9
Velocity [km/s]	-7.624	-1.596	0

**Table 2.** Initial State of GOCE-like in J2000 Coordinates.



The 39th International Electric Propulsion Conference, Imperial College London

London, United Kingdom 14–19 September 2025

Page 11

Copyright 2025 by the Electric Rocket Propulsion Society. All rights reserved.

Simulations were initially conducted using the same intake diameters and efficiencies used in Ref. 7, with the success criterion defined as a flight time of 300 days. The tests were performed with control values,  $k_p$ , ranging from 0.2 to 0.5, which did not affect the success criterion. These initial simulations were carried out using only a passive intake, with the compression ratio defined by Eq. (8). However, this configuration resulted in re-entry within a short time frame for all cases. To further investigate this effect, the intake wall temperature in Eq. (8) was set independently. Lowering this value was found to be beneficial, and an extreme optimistic case was assumed using a wall temperature of 200 K. Nevertheless, even under this assumption, all cases still resulted in re-entry within a short time frame. Therefore, subsequently, all cases were assumed such that an active stage was able to provide a constant compression ratio of 300.

Furthermore, in contrast to the representative constant mass flow rate of 0.1 mg/s used in Ref. 7, the present study applied a limit of 6 sccm. Since this value varies along the orbit as a function of atmospheric composition and related effects, it was found to introduce a beneficial impact on the results. In particular, some edge cases that previously failed were able to sustain flight. For example, a configuration with an intake diameter of 45 cm and an intake efficiency of 40% aligned with VNB frame, achieved successful flight under this assumption, whereas it did not in Ref. 7. This improvement is attributed to the small but noticeable fluctuations in the required mass flow rate (expressed in mg/s), as discussed in Ref. 1. These findings highlight that many cases operate under marginal flight conditions and underscore the importance of either developing robust control methodologies or ensuring that the thrusters are capable of generating additional thrust.

The outcomes of the overall simulations are summarized in Table 3, including the corresponding attitude alignments for the case with  $k_p > 0.3$ . In the VNB alignment case, the intake collection efficiency was also varied with respect to the angle as described in Sec. III. It can be observed from the table that attitude alignment influenced the orbital performance: in several cases the VNB alignment resulted in mission failure, whereas the attitude aligned with WRF enabled sustained flight. One such case is illustrated in Fig. 8, corresponding to a spacecraft with a 36 cm inlet diameter and 45% intake efficiency. It should be noted, however, that in all of these tests the thruster was assumed to fire along the spacecraft body axis. Consequently, for the VNB alignment a thrust-vector misalignment exists, which may have contributed to the unfavourable results. This aspect could be investigated and mitigated further in future work by considering thrusters with adjustable tilt. However, this was beyond the scope of the current research.

Nevertheless, it was also observed that for WRF alignment under  $k_p > 0.5$  control the satellite performed

**Table 3. ABEP Simulation results for control with  $k_p > 0.3$**

Intake Diameter	Attitude Alignment	Efficiency ( $\eta_{c,0}$ )	Success	Mean Altitude [km]
36 cm	VNB & WRF	0.50	Success	205
	WRF	0.45	Success	200
	VNB	0.45	Fail	N/A
45 cm	VNB	$\eta_c \in [0.40, 0.50]$	Success	210-220
	WRF	$\eta_c \in [0.40, 0.50]$	Success	215-220
50 cm	VNB & WRF	$\eta_c \in [0.40, 0.45]$	Success	220
	VNB & WRF	0.30	Fail	N/A
	WRF	0.35	Success	215
	VNB	0.35	Fail	N/A
55 cm	VNB & WRF	0.40	Success	225
	VNB & WRF	0.30	Fail	N/A
	WRF	0.35	Success	220
	VNB	0.35	Fail	N/A
60 cm	VNB & WRF	$\eta_c \in [0.35, 0.40]$	Success	225-230
	VNB & WRF	0.30	Fail	N/A



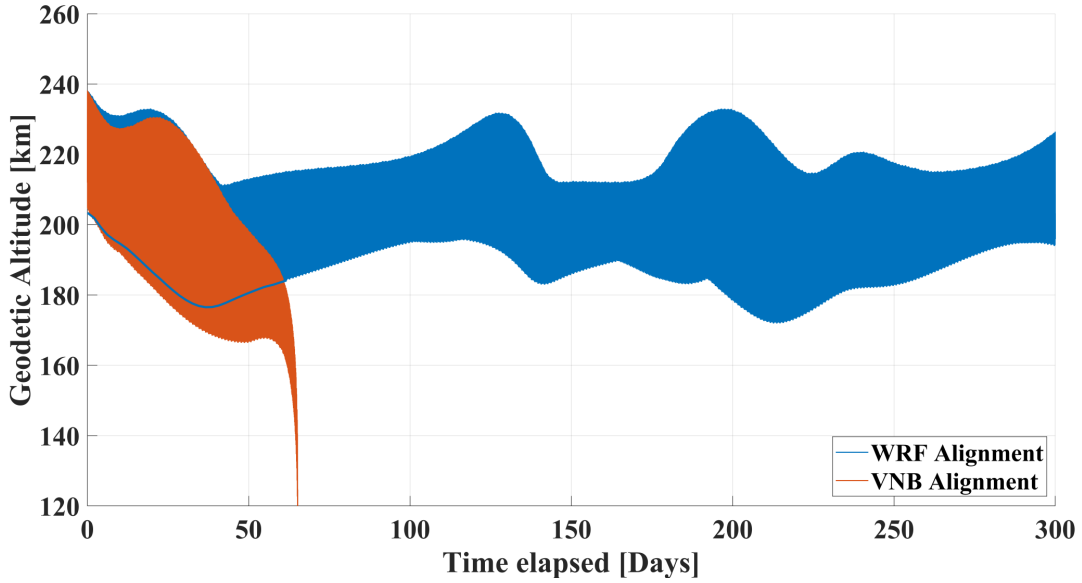


Figure 8. Comparison of WRF and VNB alignments for the GOCE-like satellite with 36 cm diameter and 45% intake efficiency.

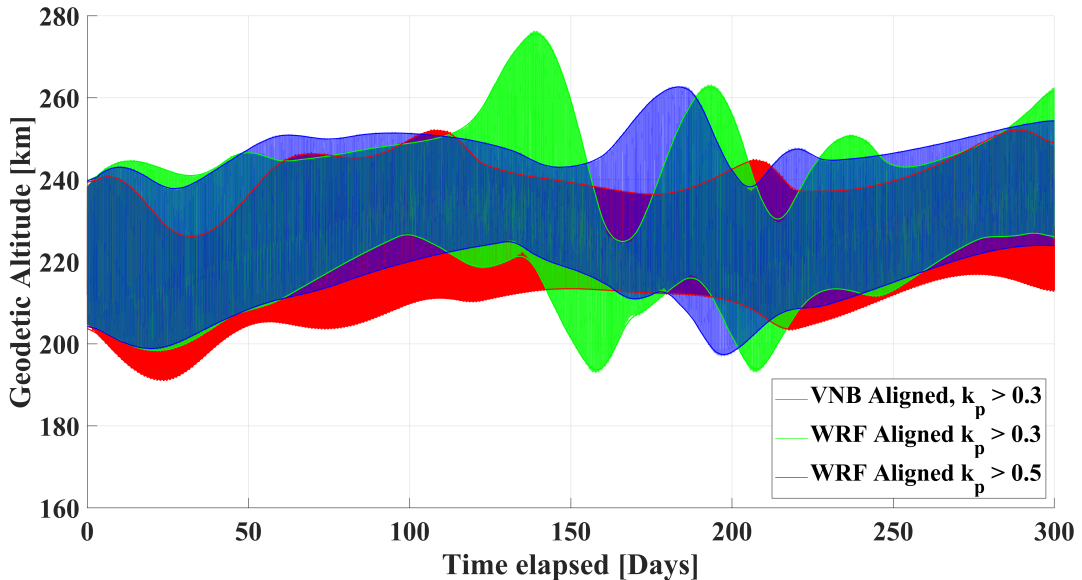


Figure 9. Effect of control parameter on WRF and VNB alignments for a GOCE-like satellite with 60 cm diameter spacecraft and 35% intake efficiency.

more stably, as the orbit exhibited less variability in altitude, although this did not alter the overall success criterion. This is illustrated in Fig. 9 for a spacecraft with a 60 cm inlet diameter and 35% intake efficiency. Moreover, while the WRF alignment was generally more successful, the methodology of the  $k_p$  control, assuming perfect alignment with the VNB frame, appeared to negatively influence orbital stability. In particular, in cases where both alignment strategies resulted in sustained flight, the WRF frame was more susceptible to destabilization, with the orbital eccentricity exhibiting significant variation over the 300-day period. A more detailed investigation of this effect is left for future work.

## V. Flight Simulation and Orbit-Keeping of EULO

### A. Aerodynamic Analysis

The aerodynamics of the EULO spacecraft, described in Sec. II, were first investigated using a Test Particle Monte Carlo (TPMC) simulation performed with SPARTA.<sup>22</sup> The test particle method was preferred over the Direct Simulation Monte Carlo (DSMC) approach, as it was computationally faster. Although initial trials were conducted at an altitude of 200 km, it was found that compensating for the total drag at this altitude would be unfeasible for the spacecraft. Consequently, the analysis was carried out at a target altitude of 240 km, identified as an approximate equilibrium point between available thrust and atmospheric drag, and this altitude is adopted throughout this section. Moreover, in order to simplify and align with the previous methodologies the intakes were completely blocked and assumed to be flat plates with 0% collection efficiency.

TPMC simulations were performed using the conditions summarized in Table 4, employing a Maxwellian reflection model with an accommodation coefficient of 0.9 and a wall temperature of 400 K. To ensure statistical convergence, the simulations were continued until a steady state was reached, defined as the point where the drag coefficient curve over time exhibited a stable plateau. After this point, results were averaged over an additional 400,000 time-steps to improve accuracy. All aerodynamic forces were reported in terms of non-dimensional force coefficients, obtained by normalising the computed forces with respect to the reference area of  $2.14 \text{ m}^2$ .

The conditions used for the TPMC simulations were also applied to the Ray Tracing Panel (RTP) method, which is the panel model with shadowing enabled, in order to provide a direct comparison. The RTP analysis was carried out on three different surface meshes of increasing resolution, ranging from 10,000 to 145,000 elements. In all cases, small but noticeable discrepancies were observed in the results, caused mainly by shadowing effects. A key issue identified was that the RTP method consistently failed, regardless of mesh resolution, when the spacecraft was perfectly aligned with the flow at 0 degrees Angle of Attack (AoA). This limitation was traced to the original shortcoming of the ray-tracing algorithm, as was also discussed by their developers in Ref. 14. The corresponding results of this aerodynamic analysis are shown in Fig. 10 (a) where the force coefficients were normalised into a single dimension for representation purposes. To ensure the overall aerodynamic trends remained visible in the figure, additional RTP cases were computed at a very small incidence ( $\text{AoA} = 0.001^\circ$ ).

Nevertheless, the sudden and unstable behaviour noticed at the  $0^\circ$  flow incidence motivated a more detailed investigation into the ray-tracing procedure, which revealed that at shallow incidence angles (below  $2^\circ$ ) the bottom part of the solar panels located on the rear of the spacecraft were incorrectly identified as non-shadowed. This artefact was addressed by excluding such panels from the analysis, since under the small incidence angles considered in this study they would in practice be fully occluded. These aerodynamic results are shown in Fig. 10 (b).

To investigate the impact of applying the shadowing approach for  $0^\circ$  incidence, Blender<sup>23</sup> was used to identify the shadowed surface areas, which were subsequently excluded from the aerodynamic computation. For incident flow at  $0^\circ$  angle of attack, the resulting force coefficient was found to be considerably lower than the surrounding cases, as highlighted by the green star in Fig. 10. To further analyse this shadowing effect, the 42k-element mesh model was employed in TPMC to obtain the average aerodynamic force acting on each mesh element. These values were also computed over the course of the simulation and subsequently averaged across 400,000 time-steps after steady state had been reached. For visualization, the elemental forces were normalized and clamped such that their total contribution summed to 99% of the overall force.

**Table 4. Flow conditions and species composition used in the TPMC**

Flow conditions		Species composition	
Flow velocity	7760.7 m/s	He	0.24%
Flow temperature	921 K	O	70.31%
Flow density	$2.53 \times 10^{15} \text{ m}^{-3}$	N <sub>2</sub>	27.93%
Reference area	$2.14 \text{ m}^2$	O <sub>2</sub>	0.89%
		N	0.61%



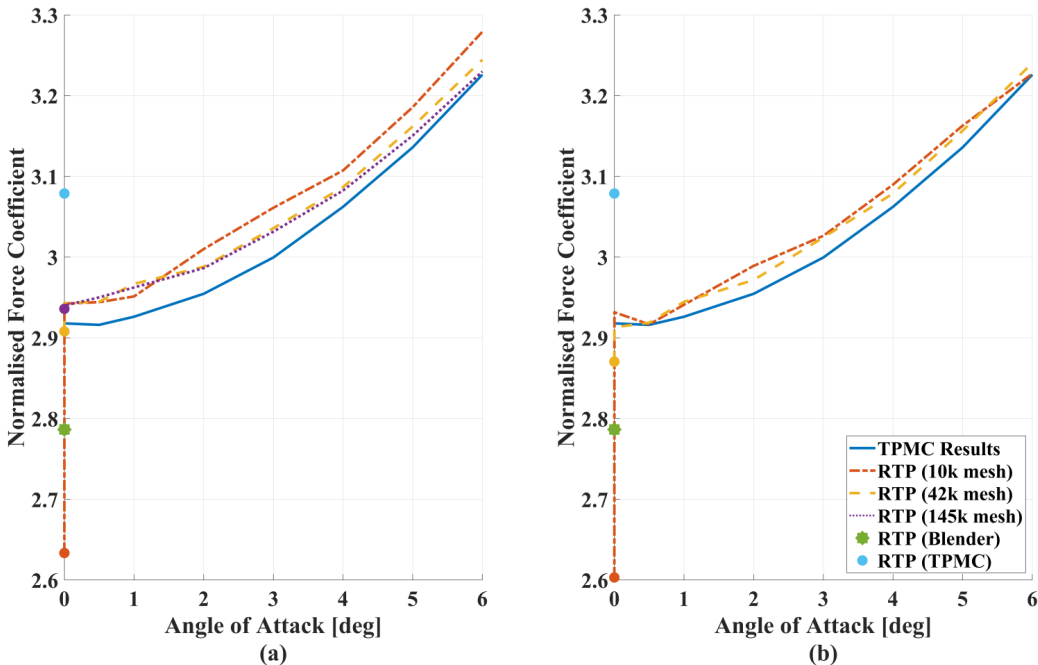


**Figure 10.** Comparison of single-dimensional force coefficients of EULO spacecraft versus angle of attack with different methods and approaches as described in the text.

The resulting distribution, is presented on a logarithmic scale as an overall combination of shear stress and pressure in Fig. 11 (a).

It was observed that although most of the spacecraft body is shielded from the free stream by the nose cone, the TPMC results indicate that particles still reach these regions through thermal motion or gas–surface scattering mechanisms, with the exception of a small area immediately behind the intake unit which remains fully shielded. This behaviour highlights an inherent limitation of the RTP approach, which assumes complete occlusion of such surfaces. Similarly, Fig. 11 (b) presents the corresponding panel estimation without shadowing effects for the same simulation condition. In this case, the overall magnitudes predicted without shadowing are broadly consistent with the TPMC results, except in the intake channels where multiple scattering effects lead the panel method to misrepresent the forces. The overall force coefficient obtained from the panel method by removing the TPMC identified shadowed regions is also shown in Fig. 10, marked by the blue dot.

Similarly, the case with a  $3^\circ$  angle of attack was also analysed. The results are shown in Fig. 12 (a) for TPMC and Fig. 12 (b) for the RTP method. Comparable trends to  $0^\circ$  case were observed at the intake channels, where multiple scattering effects again play a significant role in the differences between the two approaches. In addition, small disruption patterns appear on the inlet in the RTP results, caused by the shadowing algorithm incorrectly identifying certain surfaces as occluded and removing them from the computation.

Furthermore, differences were observed on the upper surface ( $+z$ ), where the RTP method again produced shadowing behaviour that differed from the TPMC results. This discrepancy can be attributed to the same artefacts noted in earlier cases. By contrast, the bottom surface ( $-z$ ) generally showed good agreement, apart from a small region missed in the RTP computation. It is also worth noting that when shadowing was evaluated separately using Blender, the entire bottom surface was marked as shadowed. Since “shadow” in the RTP method corresponds strictly to an occlusion check, this treatment is not fully accurate, as such surfaces clearly still contribute to the aerodynamics, as confirmed by the TPMC results. These effects are left for future investigation, as they fall beyond the scope of the present paper.

Overall, the comparison shows that the results remain within a 1% relative error margin. This residual difference likely arises from the combination of an underprediction of the forces in the intake unit and an overprediction on the side panels. For reference, at  $0^\circ$  angle of attack, the TPMC results and the panel



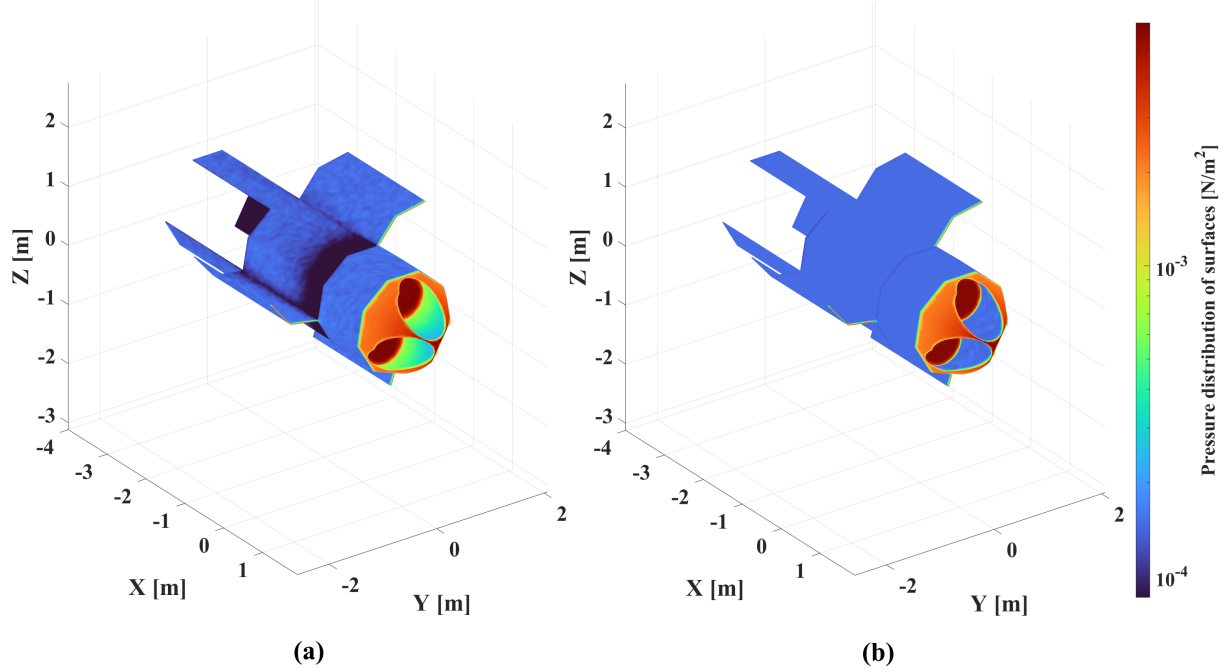


Figure 11. Combined aerodynamic shear & pressure distribution from the (a) TPMC & (b) Panel Method of the EULO spacecraft at  $0^\circ$  angle of attack.

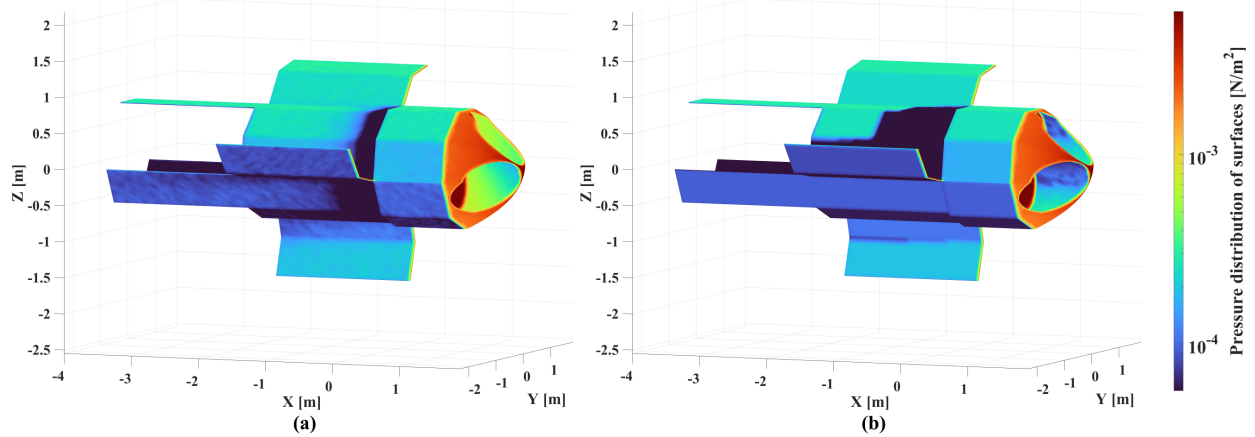


Figure 12. Combined aerodynamic shear & pressure distribution from the (a) TPMC & (b) RTP Method of the EULO spacecraft at  $3^\circ$  angle of attack.

method corrected with TPMC-based shadowing still differed by approximately 5% relative error.

Moreover, for cases where the rear surfaces that had been falsely flagged as non-shadowed were excluded, as shown in Fig. 10 (b), the results generally aligned within 1% relative error between the RTP and TPMC methods for both the 10k and 42k element mesh models. Although the previously discussed uncertainties remain with the RTP approach, and TPMC is inherently more reliable, performing a TPMC simulation at every step of an orbital propagation is computationally infeasible. Given the close agreement observed in the present comparisons, including the full three-dimensional force coefficients, which are not shown here, the RTP method was adopted for the subsequent analyses. For the WRF alignment, satellite shadowing was predefined, while for the VNB alignment a restriction was imposed on angles below  $0.001^\circ$ , which were instead evaluated at small non-zero angles to prevent failures of the algorithm adversely affecting the results.

## B. Flight Simulations

Building upon the orbit analysis presented in Sec. IV, the flight simulations of the EULO spacecraft were performed under the assumption that active compression would be required throughout the mission. Furthermore, as the spacecraft is equipped with three thrusters, the minimum mass flow, and thrust were each scaled by a factor of three. The thrusters were assumed to operate simultaneously, as each thruster unit was assumed to be fed by a single intake. Therefore, even if the conditions were sufficient to operate only one or two of them, the algorithm did not trigger any thruster. This effect is beyond the scope of the present study; however, future research could investigate this aspect in more detail and propose improvements to the overall design and control of the spacecraft. For the purposes of this analysis, the thrusters were again assumed to be the RIT-10 working with N<sub>2</sub>-O<sub>2</sub> mixtures.<sup>5</sup>

The initial orbital state for the simulations was updated relative to the values used in the GOCE-like reference case, as listed in Table 5. For consistency across all simulations, the control with a  $k_p > 0.3$  was implemented. The solar and geomagnetic conditions were kept identical to those used in the earlier analyses, and the same aerodynamic and gravity models were retained.

The initial set of simulations was conducted with the attitude aligned to the WRF frame while the shadowing was predefined, as discussed in the previous section. A key issue encountered was that when DSMC-based shadowing was applied, the resulting drag was significantly higher than in any other case. Conversely, when the ray-tracing shadowing was used, the drag was considerably lower than with any other predictions, representing an overly optimistic scenario. To ensure a conservative assessment, it was therefore decided that the initial analysis would be performed using DSMC-based shadowing, representing a worst-case condition. Consistent with the previous section, a success criterion of 300 days of sustained flight was adopted.

For this analysis, the intake collection efficiency was varied between 35% and 60% in 5% increments, while the compression ratio constraint was removed. The results indicated that for efficiencies of 35%–45%, the spacecraft was unable to sustain flight, as the minimum mass flow requirement to the thrusters could not be satisfied enough to sustain the orbit. By contrast, for efficiencies of 50% and above, the spacecraft successfully maintained its orbit throughout the simulation period. To analyse the overall compression ratio, the case with 50% intake efficiency was assessed against the minimum compression required to satisfy the density flow condition. This comparison is shown in Fig. 13, where the orange line indicates the regions in which the mass flow requirement was simultaneously met. The threshold was found to lie between an overall compression ratios of approximately 560 and 600. This threshold was verified again by reintroducing the compression ratio constraint, with values ranging from 500 to 660 in increments of 33. The results confirmed that all cases with compression ratios below 566 resulted in re-entry, whereas those at or above 566 were able to sustain flight.

The same initial state was then simulated using the ray-tracing based shadowing model in WRF frame. In this case, the orbital evolution followed the same general trends as in the DSMC-based analysis, with the exception that the 45% intake efficiency case was also able to sustain flight, as illustrated in Fig. 14. Based on the DSMC results, the true performance is expected to lie between the two shadowing assumptions. Consequently, a conservative minimum intake collection efficiency of 50% needs to be targeted for the EULO spacecraft. Following these results, the analysis was extended to the VNB frame attitude alignment. Although the initial plan was to use the 42k-element mesh model, the simulations were instead carried out with the 10k-element mesh due to computational time constraints. Similar to the WRF alignment cases, the compression ratio was held constant at 566, while collection efficiencies ranging from 45% to 60% were examined. For the VNB alignment, all cases except the 45% collection efficiency configuration achieved sustained flight, consistent with the results previously obtained for the WRF frame with DSMC-based

**Table 5. Initial state of the EULO spacecraft in J2000 coordinates.**

Component	X	Y	Z
Position [km]	152.6	-729.2	6576.0
Velocity [km/s]	-7.596	-1.590	0.000
Epoch (J2000)	01 Jan 2000, 12:00 TT		



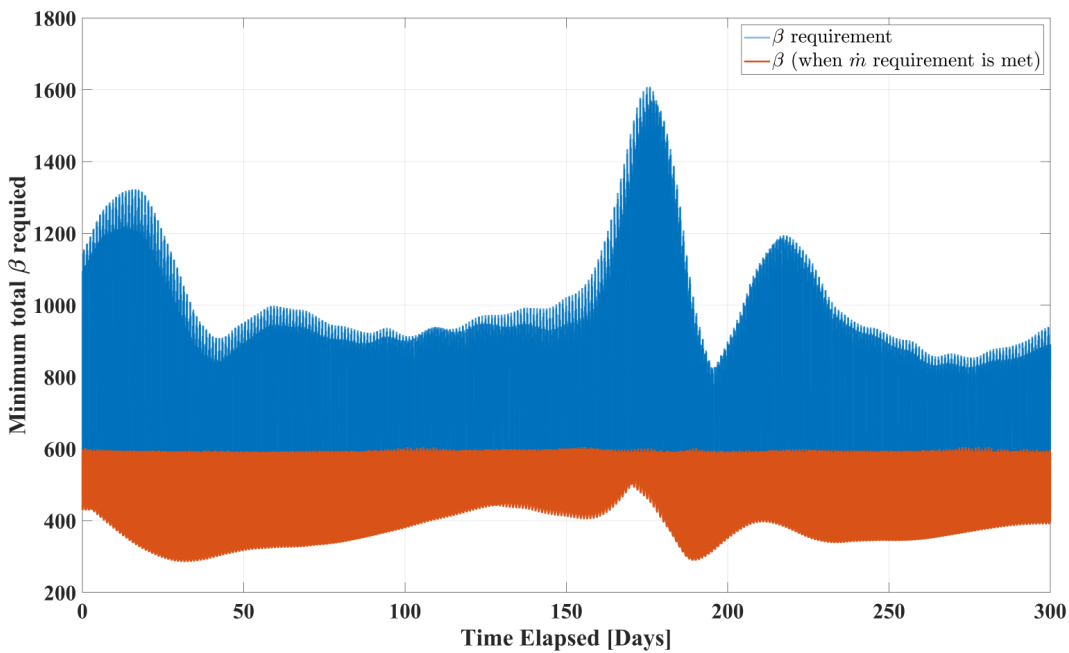


Figure 13. Variation of the minimum total compression required to meet the thruster density flow requirement for EULO with 50% intake efficiency.

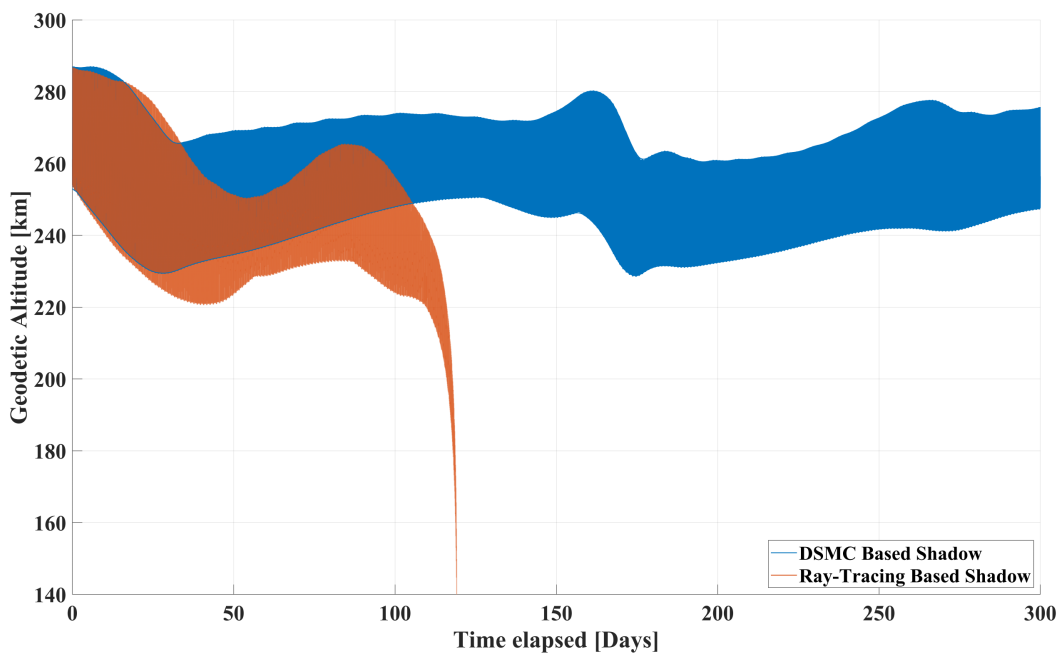


Figure 14. Orbital propagation of the 45% collection efficiency case under different shadowing assumptions.



The 39th International Electric Propulsion Conference, Imperial College London

London, United Kingdom 14–19 September 2025

Copyright 2025 by the Electric Rocket Propulsion Society. All rights reserved.

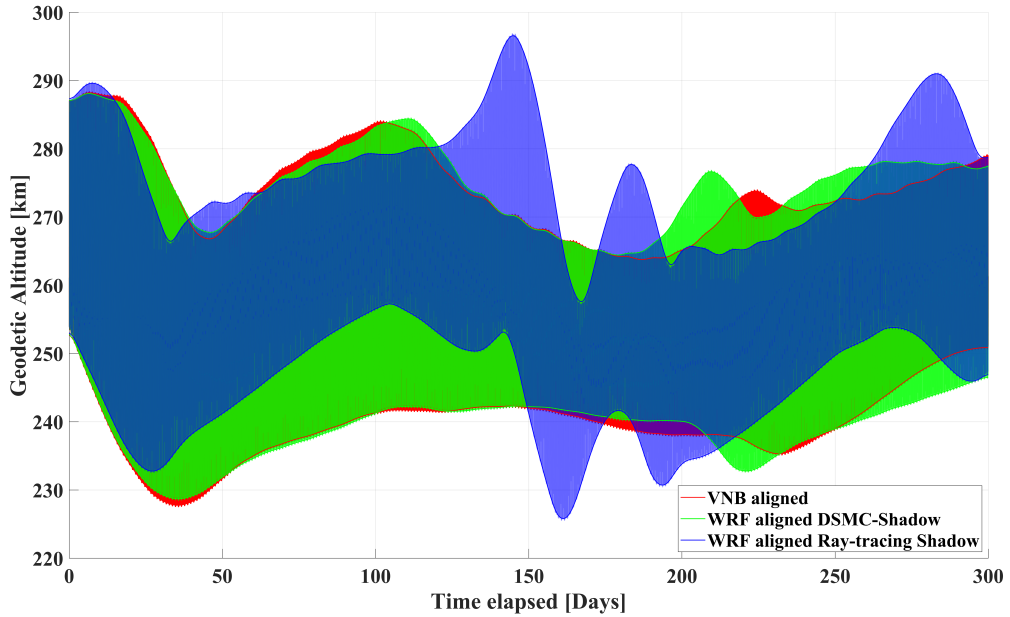


**Figure 15.** Flight envelope of the EULO spacecraft with 50% collection efficiency under different frame alignments.

shadowing.

The resulting flight envelopes for the 50% collection efficiency case are shown in Fig. 15. It can be observed that the DSMC-based shadowing case in the WRF frame and the VNB-aligned model produced similar outcomes. This similarity is attributed to the polar orbit used in the simulations, where the satellite orientation occasionally introduced misalignments of up to 4°. As a result, the aerodynamic forces in both frames evolved in a comparable manner. For completeness, the corresponding ray-tracing-based shadowing case is also included in Fig. 15. In summary, the flight simulations demonstrated that sustained operation of the EULO spacecraft is possible under the considered conditions, provided that intake efficiencies remain above 50%. Nevertheless, the assumptions adopted in this analysis represent an optimistic scenario. Given the uncertainties associated with aerodynamic drag modelling and the fact that many cases operate near the margin of feasibility, more efficient thrusters may be required in practice to ensure a successful mission.

## VI. Conclusions

This study investigated the design and feasibility of an Air-Breathing Electric Propulsion (ABEP) spacecraft initially intended for sustained operations at an altitude range of approximately 190 to 250 km. The spacecraft was specifically designed for optical Earth observation missions and sized to be compatible with launch from a UK-based launcher, RS-1. Preliminary analyses indicated that at least two thrusters would be required to meet the propulsion demands, based on existing RIT-10 performance data tested with N<sub>2</sub>-O<sub>2</sub> mixtures.<sup>5</sup> However, due to constraints on spacecraft length and the relatively large payload volume required by the optical instruments, the final design was adapted to incorporate three thrusters, each fed by an independent smaller intake system.

Due to the inclusion of three intake units, a nonagonal spacecraft body was selected with an inner diameter of 1.6 m. The solar panels were designed considering the worst-case power demand scenario; however, the body-mounted panels alone would be insufficient to supply power to three thrusters operating simultaneously. Consequently, additional deployable solar arrays were implemented. Six deployable panels were designed to fold and stow against the spacecraft body. Three of them were used as cranked panels deployed from the body while the other three panels were configured as tail units. The authors acknowledge that the tail-mounted panels may be subject to plasma plume interactions caused by the electric propulsion system. This effect was beyond the scope of the present study and is identified as an area for future research,



which may lead to further design modifications. However, in its current configuration, these deployable tail units could also serve as aerodynamic brakes or as control surfaces for attitude management.

Previously developed orbital propagator for Very Low Earth Orbit (VLEO)<sup>7</sup> was enhanced with a faster pseudo-shadowing algorithm by incorporating a bounding volume hierarchy (BVH) logic into the original approach proposed by Ref. 14, enabling a faster assessment of complex meshes. In addition to the velocity–normal–binormal (VNB) frame alignment used in the previous study,<sup>7</sup> a new attitude strategy was investigated in which the satellite is assumed to be perfectly aligned with the instantaneous free-stream velocity. Furthermore, this study introduced a simple variability in the intake collection efficiency due to flow misalignment, and switched from a fixed mg/s mass flow rate to an sccm based mass flow limit, which yielded more favourable results compared to the prior work.<sup>7</sup> Similarly, limits on mass flow and number density was also imposed on the thrusters.

The generic assessment of an ABEP spacecraft using a GOCE-like shape revealed that some orbits were only marginally stable, with the flow angles induced by the VNB frame alignment causing the satellite to de-orbit, whereas the same scenario in the WRF frame sustained flight. This emphasizes the importance of proper satellite flow alignment. It should be noted that, due to the polar orbit employed, these angles varied by up to approximately 4°, primarily as a result of the Earth’s co-rotation. The authors also acknowledge that these cases were controlled with a misaligned thruster, since the thruster is body-mounted; providing the thruster with an independent degree of freedom could modify the results. Furthermore, similar to the previous study,<sup>7</sup> the present analysis also highlighted that a passive intake collection unit alone may not be sufficient to sustain the satellite’s orbit.

The ABEP spacecraft EULO, designed in this study, was analysed for aerodynamic performance using both TPMC and panel-based methods. During the design phase, it became evident that a larger satellite configuration than originally planned was required. Consequently, the minimum altitude at which EULO was capable of sustaining flight was found to be approximately 240 km, based on the balance between total thrust and aerodynamic drag. Therefore, the aerodynamic analysis were performed assuming a representative atmospheric environment at 240 km.

The aerodynamic investigation using the ray-tracing panel (RTP) method revealed that, as previously noted by the original developers,<sup>14</sup> the pseudo ray-tracing model failed under zero-degree flow incidence. To assess the aerodynamics using a panel-based approach, Blender<sup>23</sup> was employed to identify shadowed areas and manually remove panels that were occluded according to the shadowing algorithm. However, comparison with the TPMC analysis highlighted a limitation of panel methods: components located behind the nose cone, which should have been fully shadowed, were still predicted to experience aerodynamic forces, potentially due to thermal motion of particles and multiple scattering effects.

Subsequently, an alternative shadowing approach was applied by removing parts of the CAD model that were predicted to contribute less than 1% of the overall aerodynamic pressure by a TPMC simulation. Unfortunately, both the original and modified approaches either under- or over-predicted the aerodynamic forces. Conversely, for angles above 0.001°, the RTP method produced predictions with approximately 1% relative error. Nevertheless, it must be noted that panel-based approaches fail to capture double-scattering behaviour, which was clearly exhibited in the TPMC results, and the precise shadowing mechanism still differed between the TPMC and RTP methods.

Nonetheless, as it was computationally infeasible to use a TPMC simulation within the orbital propagator, a panel-based approach was employed. In this method, a limitation was introduced to prevent the flow angle from approaching zero by effectively imposing small angle perturbations below a defined threshold. All aerodynamic models and frame alignments were tested using the control methodology previously suggested by Ref. 7 with the same constant solar weather conditions. It was observed that, for the satellite to sustain flight, the intake efficiency must be at least 50% for reliability. Although the ray-tracing-based WRF shadowing correction enabled the satellite to successfully complete 300 days in orbit with 45% collection efficiency, the results showed roughly a 5% relative error on aerodynamic force compared to the TPMC predictions. Therefore, it is safer to assume a minimum collection efficiency of 50%. Additional investigations were conducted by removing the number density requirement from the thruster. This analysis indicated that a compression ratio of approximately 566 is required for the satellite to maintain its orbit, which was subsequently verified through orbit simulations.

For the EULO spacecraft, the mean operational altitude was approximately 255 km across the different simulated cases. Consequently the ground sampling distance for the optical payload becomes 0.38 m. Both the WRF alignment with DSMC-based shadowing and the VNB frame alignment with shadowing produced



similar results, which is attributed to the effective flow angle reaching up to roughly  $4^\circ$  in the VNB frame alignment due to the polar orbit and the Earth's co-rotation. In contrast, for the WRF alignment using ray-tracing based shadowing, the satellite maintained the same mean altitude but exhibited a slightly lower orbital eccentricity and more fluctuation in the semi-major axis. These results indicate that there are significant uncertainties associated with the ABEP spacecraft orbits. To mitigate the fluctuations and uncertainties caused by drag prediction, density modelling, and related factors, it would be beneficial to improve thruster efficiency, allowing for a reduction in solar panel area.

Furthermore, the requirement for high compression ratios suggests that these thrusters could benefit from operation at lower plasma densities. This could potentially allow the use of purely passive intake units; however, even with 50% collection efficiency, alternative materials would likely be needed for the intakes to create specular reflections which could potentially enable these collection efficiencies.

## Acknowledgments

This paper presented the outcomes of various ABEP development activities carried out at the Surrey Space Centre (SSC) with funding from the United Kingdom Space Agency (UKSA)'s Enabling Technologies Programme under project "EULO". Additionally, Hamza Eren Gunaltay would like to express sincere gratitude to the University of Surrey and Surrey Satellite Technologies Ltd. (SSTL) for funding their PhD research.

## References

- <sup>1</sup>Tisaev, M., Ferrato, E., Giannetti, V., Païsonni, C., Baresi, N., Lucca Fabris, A., and Andreussi, T., "Air-breathing electric propulsion: Flight envelope identification and development of control for long-term orbital stability," *Acta Astronautica*, Vol. 191, 2022, pp. 374–393.
- <sup>2</sup>NASA Goddard Space Flight Center, "General Mission Analysis Tool (GMAT)," 2023, Accessed: 2024-12-16.
- <sup>3</sup>Crisp, N., Roberts, P., Livadiotti, S., Oiko, V., Edmondson, S., Haigh, S., Huyton, C., Sinpetru, L., Smith, K., Worrall, S., Becedas, J., Domínguez, R., González, D., Hanessian, V., Mølgaard, A., Nielsen, J., Bisgaard, M., Chan, Y.-A., Fasoulas, S., Herdrich, G., Romano, F., Traub, C., García-Almínana, D., Rodríguez-Donaire, S., Sureda, M., Kataria, D., Outlaw, R., Belkouchi, B., Conte, A., Perez, J., Villain, R., Heißerer, B., and Schwalber, A., "The benefits of very low earth orbit for earth observation missions," *Progress in Aerospace Sciences*, Vol. 117, 2020, pp. 100619.
- <sup>4</sup>Gini, F., Otten, M., Springer, T. A., Enderle, W., Lemmens, S., and Flohrer, T., "Precise Orbit Determination of the GOCE Re-Entry Phase," Tech. rep., European Space Agency (ESA), 2015, Accessed: 2024-12-15.
- <sup>5</sup>Lotz, B., Collingwood, C., and Feili, D., "Radio Frequency Ion Thrusters Operated with Non-Conventional Propellants," *Trudy MAI*, Vol. 60, 2012, Accessed: 2024-12-16.
- <sup>6</sup>Dhillon, V., "Reflectors," [http://www.vikdhillon.staff.shef.ac.uk/teaching/phy217/telescopes/phy217\\_tel\\_reflectors.html](http://www.vikdhillon.staff.shef.ac.uk/teaching/phy217/telescopes/phy217_tel_reflectors.html), 2013, Accessed: 2025-09-03.
- <sup>7</sup>Gunaltay, H. E., Lucca Fabris, A., Underwood, C., Marxen, O., Gini, F., and Baresi, N., "A high-fidelity orbit propagator and control strategy for VLEO platforms," *Proceedings of the 2nd International Symposium on Very Low Earth Orbit Missions and Technologies*, Stuttgart, Germany, January 2025.
- <sup>8</sup>ABL Space Systems, "ABL Payload User's Guide," <https://ablspacestystems.com/wp-content/uploads/2022/06/ABL-Payload-Users-Guide-2022-V1.pdf>, 2022, Accessed 2025-04-01.
- <sup>9</sup>Montenbruck, O. and Gill, E., *Satellite Orbits: Models, Methods and Applications*, Springer, Berlin, Heidelberg, 2000.
- <sup>10</sup>Kaula, W. M., *Theory of Satellite Geodesy: Applications of Satellites to Geodesy*, Dover Publications, New York, 1966.
- <sup>11</sup>for Global Earth Models (ICGEM), I. C., "ICGEM Gravity Field Service Data," 2016, Accessed: 2024-12-16.
- <sup>12</sup>Acton, C. H., "Ancillary Data Services of NASA's Navigation and Ancillary Information Facility," Tech. Rep. 44(1), Planetary and Space Science, 1996, Accessed: 2025-08-08.
- <sup>13</sup>Picone, J. M., Hedin, A. E., Drob, D. P., and Aikin, A. C., "NRLMSISE-00 empirical model of the atmosphere: Statistical comparisons and scientific issues," *Journal of Geophysical Research: Space Physics*, Vol. 107, No. A12, 2002, pp. SIA 15–1–SIA 15–16.
- <sup>14</sup>Sinpetru, L. A., Crisp, N. H., Mostaza-Prieto, D., Livadiotti, S., and Roberts, P. C., "ADBSat: Methodology of a novel panel method tool for aerodynamic analysis of satellites," *Computer Physics Communications*, Vol. 275, 2022, pp. 108326.
- <sup>15</sup>Schaaf, S. and Chambre, P., *Flow of Rarefied Gases*, Princeton University Press, Princeton, NJ, 1st ed., 1958.
- <sup>16</sup>Lapointe, J., *Adaptive Estimation Techniques for Resident Space Object Characterization*, Ph.D. thesis, 12 2016.
- <sup>17</sup>Meister, D., Ogaki, S., Benthin, C., Doyle, M. J., Guthe, M., and Bittner, J., "A Survey on Bounding Volume Hierarchies for Ray Tracing," *Computer Graphics Forum (Eurographics STAR Report)*, Vol. 40, No. 2, 2021, pp. 683–712.
- <sup>18</sup>Li, Z., Ziebart, M., Bhattacharai, S., Harrison, D., and Grey, S., "Fast solar radiation pressure modelling with ray tracing and multiple reflections," *Advances in Space Research*, Vol. 61, No. 9, 2018, pp. 2352–2365.
- <sup>19</sup>NVIDIA Corporation, *CUDA Toolkit Documentation*, 2025, Version 13.0, Accessed: 2025-09-01.
- <sup>20</sup>FUJITA, K., "Air-intake Performance Estimation of Air-breathing Ion Engines," *Transactions of the Japan Society of Mechanical Engineers Series B*, Vol. 70, No. 700, 2004, pp. 3038–3044.
- <sup>21</sup>Schaub, H. and Junkins, J. L., *Analytical Mechanics of Space Systems*, AIAA, 2003.



<sup>22</sup>Plimpton, S. J., Moore, S. G., Borner, A., Stagg, A. K., Koehler, T. P., Torczynski, J. R., and Gallis, M. A., "Direct Simulation Monte Carlo on Petaflop Supercomputers and Beyond," *Physics of Fluids*, Vol. 31, No. 8, 2019, pp. 086101.

<sup>23</sup>Blender Foundation, "Blender," <https://www.blender.org/>, Version: 4.0, Accessed: 2025-01-01.

